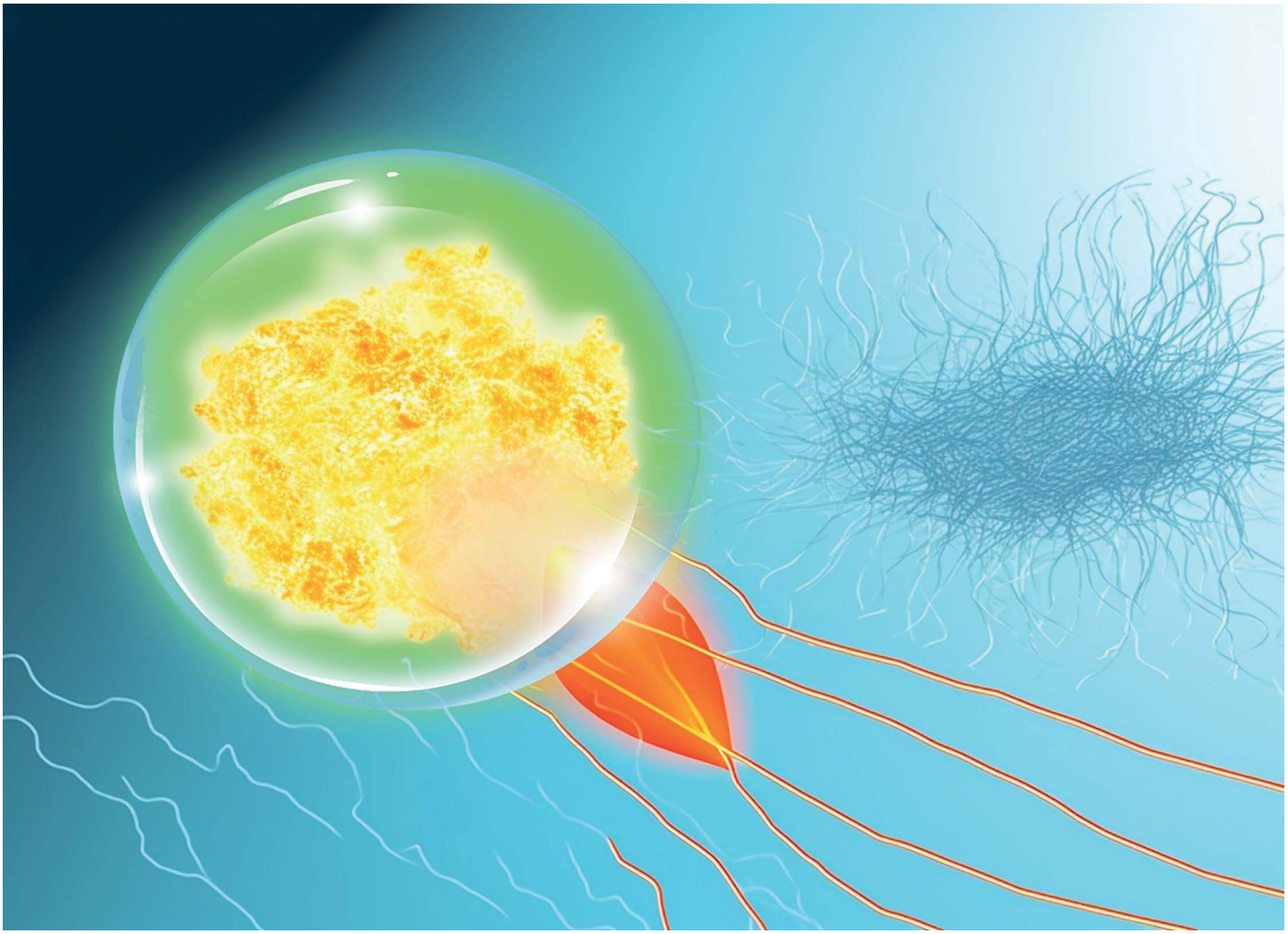

Highlighting a study on heat-resistant nanofiber membranes by a group of researchers led by Professor Yingde Wang and Professor Bing Wang from National University of Defense Technology, China.

An *in situ* hyperconnective network strategy to prepare lanthanum zirconate nanofiber membranes with superior flexibility and toughness

We report a scalable approach of sol-gel electrospinning to synthesize flexible and tough $La_{1.85}Al_{0.15}Zr_2O_7$ nanofiber membranes involving self-assembled 3D networks. The interactions between nanoscale constituents lead to high nodal connectivity and strong crosslinking, which may promote an enhancement of macroscopic mechanical properties by orders of magnitude. Mechanistic insights and manufacturability provided by these nanofiber membranes may create further opportunities for materials design and technological innovation.

As featured in:

See Bing Wang, Yingde Wang *et al.*, *J. Mater. Chem. A,* 2023, **11**, 12735.

ROYAL SOCIETY OF CHEMISTRY

rsc.li/materials-a

Registered charity number: 207890

Journal of Materials Chemistry A

ROYAL SOCIETY OF CHEMISTRY

PAPER

View Article Online
View Journal | View Issue

Cite this: J. Mater. Chem. A, 2023, 11, 12735

An *in situ* hyperconnective network strategy to prepare lanthanum zirconate nanofiber membranes with superior flexibility and toughness†

Nana Xu,‡ Xiaoshan Zhang,‡ Haiyan Liu, Hui Xu, Shuang Wu, Bing Wang* and Yingde Wang *

Oxide ceramic fibers with softness and toughness are key materials in emerging fields like wearable devices and membrane technologies. However, the brittle failure of oxide ceramic fibers after thermal cycling leads to the loss of membrane architectures, which limits their long-term applications at high temperature. Here, we report a scalable approach of sol–gel electrospinning to synthesize a flexible and tough pyrochlore $La_{1.85}Al_{0.15}Zr_2O_7$ (L5AZO) nanofiber membrane (NFM) involving self-assembled 3D networks. The interactions between the nanoscale constituents lead to the assembled networks with high nodal connectivity and strong crosslinking between nanofibers, which may promote an enhancement of macroscopic mechanical properties by orders of magnitude. Ultrasonic dispersion and an amorphous secondary phase drive the formation of numerous L5AZO nuclei and soft grain boundaries, thus effectively refining grains and inhibiting crystallite growth. Indeed, the L5AZO NFM achieves both a high specific tensile modulus of ~11.4 MPa cm^3 g^{-1} and fracture toughness of ~1032 J m^{-2}, as well as high-temperature resistance above 1100 °C, which are advantageous for diverse structural applications. Furthermore, the simple processing technique of the NFM allows it to be fabricated into various functional devices, such as aerogels, thermal camouflage, and filtration membranes at high temperature. The mechanistic insights and manufacturability provided by this flexible and tough oxide NFM may create further opportunities for materials design and technological innovation.

Received 30th November 2022
Accepted 27th February 2023

DOI: 10.1039/d2ta09347b

rsc.li/materials-a

10th anniversary statement

Congratulations on the tenth anniversary of *Journal of Materials Chemistry A*. In the past 10 years, JMCA has shared a lot of interesting innovative and enlightening scientific research among researchers and readers. JMCA also has made remarkable contributions as an excellent platform for the sharing of scientific research and communication of creative ideas. We would like to hereby express our sincere thanks for editors and reviewers' great efforts in bringing this impressive achievement. Polymer-derived ceramic fibers are the main interest of my team over the past 40 years. Our studies have earned worldwide reputation with more than 150 articles and reviews published in high-level scientific journals over the past decade. Among them, nine articles have been published in JMCA, one of which (*J. Mater. Chem. A*, 2018, **6**, 516–526) has been recognized as top 1‰ ESI. My team and I have always been willing to cite and study the work published in JMCA owing to the high quality of studies and sound academic influence. We would like to thank JMCA again for providing an excellent platform for publication and communication, and wish JMCA greater success in the future.

1. Introduction

As a kind of advanced functional ceramic materials, multi-element oxide ceramics of $A_2B_2O_7$ with pyrochlore or defective fluorite structures are widely used in thermal barrier coatings, refractories, high-temperature solid electrolytes and radioactive nuclear waste, because of their high melting point, good oxidation resistance, excellent insulating performance and low thermal expansion coefficient.[1,2] Particularly, lanthanum zirconate ($La_2Zr_2O_7$) shows a low thermal conductivity of 1.2 W m^{-1} K^{-1} and excellent thermal stability with no phase transition occurring below the melting temperature of 2300 °C, and is an ideal material for oxide ceramic fibers in multiple fields, such as in flexible sensors, high energy-density solid-state batteries, heat insulators or carriers of catalysts.[3–6] Compared with the commonly used oxide ceramic fibers, such as SiO_2, ZrO_2 and mullite fibers, $La_2Zr_2O_7$ fibers with low sintering ability will not be limited by their poor thermal stability or high thermal conductivity at high temperatures.[7,8]

Science and Technology on Advanced Ceramic Fiber and Composites Laboratory, College of Aerospace Science and Engineering, National University of Defense Technology, Changsha 410073, China. E-mail: wangyingde@nudt.edu.cn; bingwang@nudt.edu.cn

† Electronic supplementary information (ESI) available. See DOI: https://doi.org/10.1039/d2ta09347b

‡ Nana Xu and Xiaoshan Zhang contributed equally to this work.

Electrospinning generally produces a nonwoven fibrous mesh with a typical pore size of about 2–5 μm, which has wide application in filtration, separation or heat insulation.[9] Usually, oxide ceramic nanofiber membranes (NFMs) depend on the electrospinning technique to realize the ultrafine diameter and favorable size-related properties.[10,11] Nevertheless, lower mechanical resistance and larger specific surface area of nanofibers (NFs) cause rapid grain growth at much lower temperatures than that in bulk materials. Then, the rapid grain growth will lead to the disappearance of any favorable size-related properties and easy fracture of fibers.[12,13] Numerous efforts for the enhancement of oxide NFs have been devoted to suppressing the grain growth thermodynamically *via* reducing grain boundary energy as the driving force or kinetically *via* the secondary phase interface and the solute drag effect.[14–16] Additionally, achieving a high mechanical strength with currently available chemistries remains difficult due to the weak interactions among NFs.[17,18] Currently, there are several research studies about $La_2Zr_2O_7$ nanofibers (LZO NFs) by electrospinning. In order to obtain LZO NFs with high performance, achieving relatively lower sintering ability and fracture toughness (around 0.9–1.3 MPa $m^{1/2}$) of $La_2Zr_2O_7$ ceramics deserves more attention.[19] Under the dual blessing of difficult sintering and rapid grain growth, it is difficult for LZO NFs to maintain their mechanical strength at high temperatures. Among the previous studies, the adjustment of compositions or microstructures for the LZO NF material cannot significantly enhance the performance.

Li *et al.*[20] prepared LZO NFs with a low sintering ability by calcination of the electrospun fibers of the PVP-precursor, which may have potential application as a catalyst-support at high temperatures. Wang *et al.*[21] studied the effects of firing temperature (800–900 °C) on the phase and microstructure evolution of the LZO NFM. Ou *et al.*[22] tuned the ratio of defect fluorite and pyrochlore phases and further demonstrated that a LZO NFM with a mixed phase structure has higher conductivity due to an interface lattice mismatch between the two phases, which makes them a promising material for high-performance SOFCs and oxygen sensors. Jing *et al.*[23] fabricated the LZO NFM which can significantly increase the room-temperature electrochemical performance of the ultra-thin composite solid electrolyte, and is expected to be widely applied in high energy-density solid-state batteries. Yu *et al.*[24] used the harmonious activity of the mixed phase of pyrochlore/defect fluorite-structured LZO NFs to generate an interface that aids in increased electrocatalytic activity by enriching oxygen vacancies in the system, improving the photoelectrochemical ammonia production performance by coupling oxygen-vacant sites to the 2D-semiconductor based electrocatalysts. Moreover, other efforts[4,19,25] have been made to study the effects of the La/Zr source, electrospinning parameters and heat treatment conditions on the crystal growth of LZO NFs. Besides, high-entropy composites are also one of the frontier research directions of LZO NFs, striving to strengthen their function or couple them with other functional materials. Yang *et al.*[26] studied the crystal structure of pyrochlore in the La sites, which is doped to produce a $(La_{0.2}Sm_{0.2}Eu_{0.2}Gd_{0.2}Tm_{0.2})_2Zr_2O_7$ NFM, and the solid thermal conductivity of the fibers is as low as 0.23 W m^{-1} K^{-1} after heat treatment at 1000 °C. Zhao *et al.*[27] used the electrospinning technique to prepare a $Li_{6.4}La_3Zr_2Al_{0.2}O_{12}$ NFM for solid-state batteries due to its high ionic conductivity and chemical/thermal stability. Sharma *et al.*[28] fabricated elastic, well-aligned ceramic LLZO NFM based electrolytes toward high safety and high energy density solid-state Li-batteries. The above studies investigate the preparation and application of the LZO NFM in multiple directions and verified efficient properties in the areas of sensors, high energy-density solid-state batteries, heat insulators or carriers of catalysts, but its reusability, mechanical properties and high-temperature resistance cannot be achieved from these research studies.

Inspired by biomacromolecules such as cellulose and chitin, their mechanical properties can be affected by the network formed from distinct chemical crosslinking between NFs, even with similar levels of solid content.[29,30] It is conceivable that distinct crosslinking between NFs may affect the mechanical properties of the network.[31] However, the design of rigid nodes between ceramic NFs can also have a negative impact on the mechanical flexibility of a ceramic NFM. Here, we report a LZO NFM from lanthanum zirconate nanofibers (LZO NFs) with outstanding mechanical properties and excellent high-temperature resistance (above 1100 °C), through the co-design of a fibrous network and microstructures of NFs. Through the regulation of precursor sol containing aluminum, a hyperconnective network and crystal growth control can be realized. Oxide aluminum sol with chemical stability will not react with La/Zr precursors, and has low solubility in oxides (YSZ, ZrO_2, and $La_2Zr_2O_7$).[12,32] Furthermore, alumina can stay in the amorphous phase at relatively high temperatures. The unique interactions between nanoscale constituents lead to assembled 3D networks with high nodal connectivity and strong welded connection between NFs. These features lead to unusually high stiffness and strength of the NFM, which is confirmed by theoretical simulation of 3D fibrillar networks. Moreover, successive breakage of crosslinks at high connectivity nodes affords energy dissipation while maintaining the overall structural integrity. As a result, the fracture toughness of the NFM (~167 J m^{-2}) could be orders of magnitude higher than many existing NFMs. Hence, the NFMs do not break during bending and could recover automatically after releasing stress, showing significant softness and toughness compared to traditional ceramics, indicating their potential applications in wearable devices and membrane technologies.

2. Experimental

2.1. Preparation of LZO and LAZO NFMs

In order to fabricate the LZO and LAZO NFM, lanthanum nitrate (AP, Sinopharm Co., Ltd., China.) is used as the La source. Zirconium acetylacetonate ($Zr(acac)_4$) is chosen as the Zr source. Aluminum isopropoxide (AIP) is chosen as the Al source. Poly(vinylpyrrolidone) (PVP, $M_w = 1\,300\,000$) is used as a spinning

agent to ensure electrospinning. Distilled water is chosen as the solvent due to its high dielectric constant and low boiling point. $Zr(acac)_4$, AIP, and PVP are purchased from Aladdin Chemical Co., Shanghai, China. All chemicals are used as received without further purification. In a typical process, the precursor solution is prepared by dissolving $La(NO_3)_3$, PVP, and $Zr(acac)_4$ in distilled water, and then stirring at room temperature for 6 h. To investigate the effects of the materials on the properties of LZO and LAZO NFMs, various precursor solutions with AIP contents from 0, 0.5, 1.0 to 1.5 mol are prepared, respectively. The detailed compositions of the various precursor solutions are shown in Table S1.† Then precursor fibers are electrospun on an aluminum foil collector from the precursor solution. The distance between the syringe and the collector is fixed at 16 cm, and a voltage of 18 kV is applied with a flow rate of 0.8 ml h^{-1}. LZO and LAZO NFMs are obtained by calcining the as-prepared precursor fibers in air at 900 °C for 1 h with a heating rate of 10 °C min^{-1}.

2.2. Characterization

2.2.1. Morphology and composition characterization. Scanning electron microscopy (SEM, Hitachi S4800, Japan) is used to investigate the morphology of the prepared LZO and LAZO NFMs. The composition and chemical structure of the prepared NFM is investigated *via* X-ray photoelectron spectroscopy (XPS, Thermo Scientific Escalab 250Xi machine). X-ray diffraction (XRD) patterns of the NFs are collected using a Bruker AXS D8 Advance diffractometer (Germany) with Cu Kα radiation.

2.2.2. Microstructure characterization. Fourier transforms infrared (FTIR) spectra are obtained with FTIR equipment (Frontier, PerkinElmer, USA). The microstructure is examined using transmission electron microscopy (TEM, Titan G2 60-300, USA). Thermal gravimetric analysis is performed by using a thermogravimetry-differential scanning calorimetry analyzer (TG-DSC, TG209F1, NETZSCH, Germany), at a heating rate of 10 °C min^{-1} under an air atmosphere.

2.2.3. Mechanical property test. LZO and L5AZO NFMs are reheated at various temperatures (*i.e.* 1000 °C and 1100 °C) for 1 h with a heating rate of 5 °C min^{-1} under an air atmosphere. The bending rigidity of the specimens is measured on a flexibility tester (FlexTest-F-C, Hunan Nanoup Printed Electronics Technology Co., Ltd, Hunan, China). The tensile strength of the membranes is tested by using a Testometric Micro 350 tensile tester (KES-G1, Kawabata, Japan) with a loading rate of 1 mm min^{-1}. The specimen is prepared in a size of 20 mm × 3 mm. Five specimens are cut from each membrane and tested for tensile behavior. The tensile strength (σ) is calculated by using eqn (1):

$$\sigma = F/(w \times d) \quad (1)$$

where F, w, and d are the load, width, and thickness of the specimens. The thickness of the specimens is measured by using a thickness gauge (CHY-CA, Saichen Instrucment Co., Ltd, Jinan, China).

3. Results and discussion

3.1. Processing and structures of LZO and LAZO NFMs

Fig. 1a shows the synthesis of a NFM with a hyperconnective network, including (1) the preparation of sols, (2) the formation of a hybrid NFM during electrospinning, (3) and the nucleation and growth of crystals during calcination. The physicochemical properties of the precursor sols are critical to the subsequent preparation of the nanofibrous membranes. In heterogeneous sols, zirconium acetate undergoes spontaneous self-hydrolysis and condensation reactions to form cross-linked colloids.[33] At the same time, the negatively charged oxygen groups on the surface of PVP predispose it to random complexation with metal ions (Zr^{4+}, La^{3+}, and Al^{3+}). For enhancing the homogeneity of the sol, we use ultrasonic dispersion to assist in the homogeneous dispersion of PVP in the sol to further homogenize the distribution of the inorganic complexing ions. The metal ions form a uniformly distributed adsorption layer on the PVP surface, which is assembled into nanofibers during the electrospinning process. Dynamic light scattering contributes to promoting the formation of crystal nuclei, but both the nuclei and colloidal particles will grow large with a long ball-milling time that can lead to the formation of large grains in the final LZO and LAZO NFs. To determine the best time and suitable addition of aluminum sol, dynamic light scattering is applied to measure the sizes of colloidal particles. As shown in Fig. S1,† when treated with ultrasonic vibration for 45 min, the colloidal particles of LAZO show a wide diameter ranging from 0.1 to 7.2 μm.

During the electrospinning process, the sol moved along a straight line in the initial stage and then entered an unstable whip stage when the sol moved for a certain distance, in which the trajectory is a series of spiral rings with the increase in the diameter (Fig. 1c and e). With the volatilization of the solvent, the sol is continuously stretched and refined, and finally solidified into hybrid NFs (Fig. 1b and d). In LAZO sol, the more widespread presence of hydrogen bonds further increases the viscosity and conductivity of the solution (Table S1†), allowing it to merge during the process of whipping and collecting. The formation of numerous connection points affects the topology of the assembled network, which gives the NFM unique microstructural characteristics (Fig. 1d). This process may generate nodes connected to more than four adjacent nodes. Compared with aerogels, the network junctions of fibrous membranes are all *in situ* formed. This type of node does not have an interface between different materials and therefore provides high mechanical strength welded node strength. Through controlling the stacking method, it can be realized that the fibrous membrane is anisotropic in the *XY* and *Z* directions (Fig. S2†).

Secondary phase amorphous alumina can effectivity inhibit the merging of crystals, which is beneficial for forming stable NF structures during the following high-temperature calcination (Fig. 1f). In LAZO NFs, although LZO crystals nucleated and grew, they were difficult to fuse due to the blocking effect of amorphous Al_2O_3. Here, the specimens are denoted as a flexible L5AZO NFM. The high mechanical strength and thermal

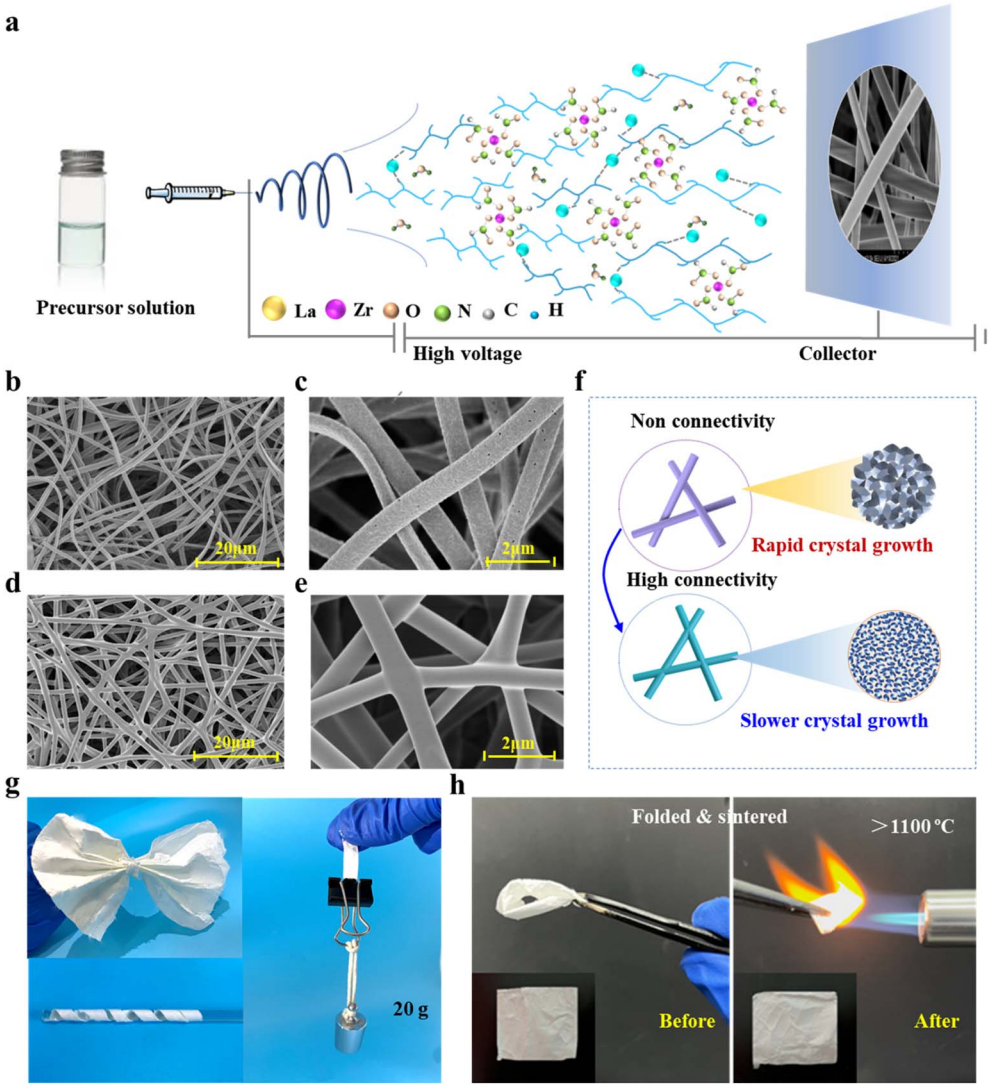

Fig. 1 Materials synthesis and characterization studies. (a) Procedures of using electrospinning followed by calcination to fabricate LZO and LAZO NFMs. (b and c) Surface morphology of the electrospun hybrid LZO NFM. (d and e) Surface morphology of the electrospun hybrid L5AZO NFM. (f) Microstructure design for LZO and L5AZO NFMs. (g) Demonstration of the flexibility of the synthesized L5AZO NFM calcined at 900 °C for 60 min. (h) Digital images of the folded and unfolded L5AZO NFM before and after calcining at 1100 °C.

stability of the L5AZO NFM allow it to be repeatedly folded under the flame of a butane torch without structural damage, demonstrating excellent flexibility and high-temperature resistance (Fig. 1h).

3.2. Influence of chemical properties on the characteristics of LZO and LAZO NFMs

During the process of precursor sol transfer into the hybrid LZO and LAZO NFMs and ceramic NFM, the growth kinetics of LZO and L5AZO NFMs is affected by crystal nucleation, grain boundary diffusion and migration. Here, alumina can enhance the conductivity and viscosity of the precursor sol so that it could be *in situ* collected into the hyperconnective NFM. Secondly, the growth and diffusion of grains can be controlled in the calcination process. Both of them can reduce defects in the precursor NFs.

To verify that the precursor sol has been modified by the aluminum sol, a series of measurements have been carried out to investigate the changes in chemical structure and composition, and the morphology of the fiber surface (Fig. 2a and S4†). Fig. 2a depicts the comparison of the FTIR spectra of pristine precursor sol and aluminum sol mixed precursor sol. The pristine precursor sol shows obvious ester absorption peaks at 3430 cm^{-1}, 2500 cm^{-1} and 1100 cm^{-1}, respectively. Moreover, a small peak at 1340 cm^{-1} is also found relative to the wagging mode of propylene.[34] The absorption peak at 3430 cm^{-1} corresponds to the stretching vibration of –OH. Additionally, after being mixed with aluminum sol, the –OH peak intensity of L5AZO is stronger than that of LZO due to the variety of oxidation. The formed –C(=O)–O–Zr– bonds show absorption peaks at 1720 cm^{-1}(C=O), 1240 cm^{-1} (C–O), 1016 cm^{-1} (La–O) and 950 cm^{-1} (Zr–O), which overlap with the peaks generated by

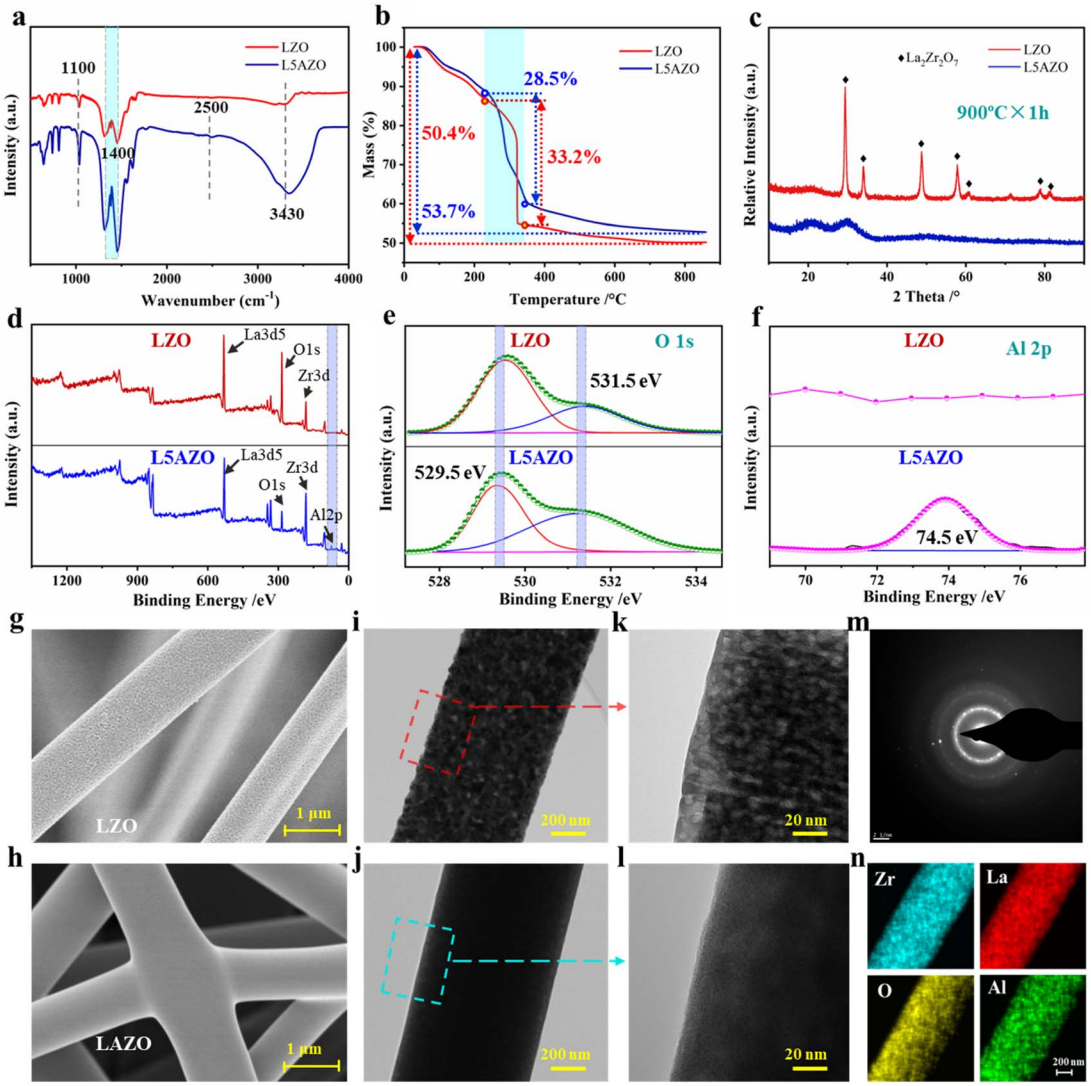

Fig. 2 Influence of the amorphous secondary phase on the morphology and flexibility of the LAZO NFM. (a) FTIR spectra of precursor sol with/without the addition of aluminum sol prepared by ultrasonic dispersion for 45 min. (b) TG curves of LZO and L5AZO precursor NFMs. (c) XRD patterns of LZO and L5AZO NFMs calcined at 900 °C. (d) XPS survey spectra of LZO and L5AZO NFMs calcined at 900 °C and peak fittings of (e) O 1s and (f) Al 2p. (g and h) Morphology of LZO and L5AZO NFMs calcined at 900 °C. (i and k) TEM of the LZO NFM after being sintered at 900 °C. (j, l and n) TEM-EDS of the L5AZO NFM after being sintered at 900 °C.

mixture precursor sol.[35] Next, thermogravimetric analysis of LZO and L5AZO precursor NFMs is illustrated in Fig. 2b, which proves the denser microstructures with a slower speed for losing weight. Furthermore, the XRD patterns of LZO and L5AZO NFMs after being sintered at 900 °C reveal the difference in phase transformation of these two kinds of NFMs. It can be inferred that amorphous Al_2O_3 surrounded $La_2Zr_2O_7$ crystals like fences, inhibiting fusing of LZO crystals and maintaining relatively lower crystal sizes (Fig. S5†).

To further demonstrate that the amorphous Al_2O_3 nanoparticles have been generated into NFs, the XPS measurements have been carried out and the results are displayed in Fig. 2d–f. Fig. 2d compares the wide scan spectra of pristine and modified NFMs. The pristine LZO NFM shows two strong peaks, corresponding to Zr 3d and O 1s, which come from $La_2Zr_2O_7$. In addition, Zr 3d and O 1s high-resolution scanning of pristine and modified TSP-PET fabrics are also tested to further compare the chemical structure before and after modification. Fig. 2e and f show the O 1s spectra of pristine and modified NFMs, respectively. The detailed O 1s spectra of the pristine NFM are fitted by two peaks, which are located at 529.5 and 531.5 eV, corresponding to O–H/O=C and the surface adsorbed H_2O, respectively.[36] When the NFM is modified by aluminum sol, another peak can be fitted at 74.5 eV, which is assigned to the Al–O–H bonds.[37] The above XPS results confirm that the L5AZO NFM has been synthesized and modified successfully.

Precursor sol with different contents of aluminum sol can be electrospun into gel NFs with smooth surfaces and similar diameters of ≈900 nm (Fig. S3†). However, after heat treatment, the NFs show different morphologies. After heat

treatment at 900 °C for 1 h, the LZO NFM showed island-shaped surfaces (Fig. 2g) because of the flow of PVP. With this template, the LZO NFM after being calcined presented discrete island-shaped surfaces with large pores. Interestingly, there are crystal grains in the LZO NFM that should be formed at higher temperatures (Fig. 2h and i). In addition, the flow of PVP on these grains left large voids in the NFs. After being calcined at 900 °C, these grains continued to grow but could not fuse well, which created a lot of pores in the LZO NFM. In contrast, the L5AZO NFM after being calcined at 900 °C for 1 h (Fig. 2k–n) is smooth and the crystals fused well without forming pores; the L5AZO NFM demonstrated superior flexibility (Fig. 1g). It has a relatively lower degree of crystallinity and homogeneous distribution of elements.

3.3. Investigation of the strengthening and toughening mechanism of the L5AZO NFM

3.3.1. Theoretical modeling. A unique feature of the L5AZO NFM is that nanofibers are connected and welded at their common joints (Fig. 3a and b), leading to high nodal connectivity in contrast to networks with a random placement of the LZO NFM. We continue to investigate how the connectivity and nodal mechanics of stochastic two-dimensional networks affect the macroscopic properties of materials. To illustrate the physical picture, it is necessary to review some established structural mechanical models of the network. In Maxwell's stiffness theory, a pin-jointed truss network exhibits finite stiffness only when its connectivity reaches a threshold of 2d, and d is the dimension of the problem. Once connectivity exceeds the critical value, the network behavior changes from fluid to solid-like. Recent studies have shown that threshold connectivity decreases if the flexural rigidity of individual fibrils is considered.[29,38] Based on these models, the random nature of fibrils and nodes in the 3D network can be considered. Secondly, the breakage of fibrillar joints plays a major role in the mechanical responses under high deformation. However, they cannot replicate the observed response of the NFM with an *in situ* hyperconnective network. Because the properties of joints and networks are parallel stacks, self-rotation also cannot be considered.

We developed a computational model to address these issues with COMSOL software. In this model, the boundary of the fibrous network stretch direction is defined by the Dirichlet boundary condition (the so-called first type of boundary condition). Then, the index strain softening

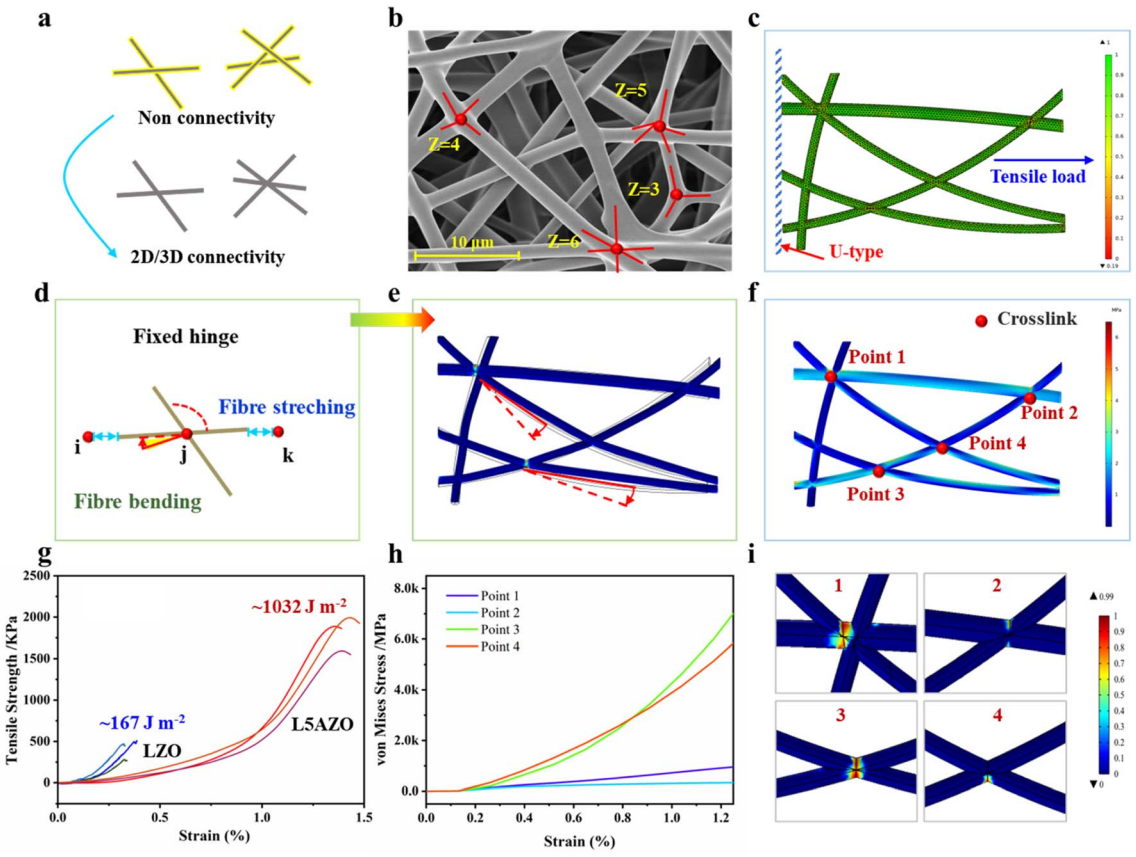

Fig. 3 Theoretical stimulation. (a) Examples of pin-jointed truss networks illustrating the distinct rigidity levels originating from different nodal connectivities. (b) SEM images and (c) the theoretical model of the NFM showing a random 2D network with various connectivity nodes. (d) A schematic model with upper parabola connecting each pair of crosslinked fibrils. (e and f) A 2D network representing strain and stress of the NFM with various connectivities. (g) Fracture characteristics of LZO and L5AZO NFMs. (h and i) Effects of the average nodal connectivity on the tensile responses of the simulated random 2D networks.

behavior is introduced to the tensile damage process of the fibrous network. During the stretching process of the fibrous network, it means that the mechanical properties of the fiber are stable when $D = 0$. If $D > 0$, it indicates that the material begins to be damaged.[39] Specifically, random placement of fibrillar segments is implemented to change the connectivity of the network to desired levels (Fig. 3c). Stochastic displacements are imposed on each node to increase the randomness of the connective network. The pull force is set parallel to the network plane, to restrain their relative separation and rotation (Fig. 3d). Young's modulus and the diameter of NFs are set to be $E = 18.2$ GPa and $d = 500$ nm, respectively, emulating the mechanics of NFs in the L5AZO NFM. In addition, breakage of the cross joints is assumed to take place once the stored elastic energy exceeds a critical value (Fig. S6†), defined as the binding energy of the cross joints.[40]The finite element method is used to simulate the response of the network under imposed strain with periodic boundary conditions. Individual NFs are modeled as 2D nonlinear Reissner beams that can undergo large stretching and bending. The lengths of NFs in each network are adjusted by a scaling factor to ensure a constant solid fraction of ~5%, corresponding to that of the L5AZO NFM (Table S2†). The elongation of the L5AZO NFM is mostly governed by the bending, enforced deformation and breakage of cross joints at nodal points, rather than the stretching and fracture of individual NFs (Fig. S6†). The mechanical energy of the network can be expressed in terms of the stretching and bending contributions of the constituent fibres. The mechanical response of such a fibre is determined by its stretching (that is, Young's) modulus, μ (units of energy/length), and bending rigidity, κ (energy × length). Broedersz[30] *et al.* found a crossover between stretching- and ending-dominated regimes characterized by an inflection in G and a strong dependence on the bond occupation probability p, or network connectivity. This suggests that the L5AZO NFM isostatic point controls a crossover between the various elastic regimes of fibril networks.

In this model, tensile moduli of the networks exhibit a strong dependence on their average nodal connectivity (Fig. 3e). After an initial linear stage, the networks experience significant strain softening, which is similar to the experimental test (Fig. 3g). More simulation results indicate that such a softening behavior is caused by the successive breakage of cross joints (Fig. 3h), which indicates that networks with high connectivity allow energy dissipation while maintaining structural integrity. From point 1 to point 4, the stress–strain curves are quite different due to the variety of connectivity and included angles. Therefore, the binding energy of cross joints plays a critical role in determining the macroscopic strength and toughness of the network. Indeed, increasing the binding energy leads to an elevated fracture strength of the material (Fig. 3i). In contrast, a lower binding energy of the cross joints will trigger an earlier softening of the material and a reduced fracture strength. These simulation results highlight the significance of welded various-connectivity joints in the L5AZO NFM for their high toughness and mechanism of energy dissipation.

3.4. Investigation of high-temperature stability and resistance of the L5AZO NFM

To further assess the thermomechanical stability of the L5AZO NFM, LZO and L5AZO NFMs are reheated to 1000 °C and 1100 °C, so as to assess their structure and performance changes after calcination. The XRD patterns of the LZO NFM and L5AZO NFM at 1000 °C and 1100 °C, present different phase evolutions, respectively, indicating the excellent thermomechanical stability of the L5AZO NFM in extreme environments (Fig. 4a and b). We calculated the average crystallite size of the L5AZO NFM and LZO NFM using the Scherer equation from X-ray diffraction and further verified these XRD crystallite sizes by direct TEM observation (Fig. 4c and e). This can be further verified by the evolution of microstructures, as shown in Fig. 4d. The growth of grain sizes and amplification of defects for the L5AZO NFM are almost constant in a wide temperature range of 900 to 1100 °C. The defects on the surface of the LZO NFM expand as the heat temperature increases, along with the increase in defect sizes and numbers.

Part of γ-alumina has been detected by XRD and TEM, which indicates the evolution of amorphous alumina to be alumina crystal. Notably, the L5AZO NFM could withstand long-term calcination at 1100 °C, showing a stable crystallite size of ~14 nm (Fig. 4j). This proves that amorphous alumina can effectively control the growth and diffusion of grains in the calcination process, and also contribute to reducing defects formed by rapid sintering. In summary, the L5AZO NFMs calcined at 900, 1000, and 1100 °C all exhibited thermomechanical stability and heat resistance with nearly zero plastic deformation after thermal recycling. By contrast, the crystallite size of the LZO NFM increased rapidly with the raising calcination temperature. When the LZO NFM was calcined at 1100 °C, $La_2Zr_2O_7$ crystallization growth cracks appeared (Fig. 4g), which usually causes matrix densification, structural collapse, and volume shrinkage of the ceramic NFM, resulting in large plastic deformation and poor elasticity of the LZO NFM. Furthermore, the mechanism of amorphous alumina on grain growth in the nanofibers is determined (Fig. 4f). Unlike the LZO NFM, rapid grain growth is not observed in the LZO NFM, neither at the surface nor in the inner part (Fig. 4d and j), thereby implying that the amorphous alumina inhibited rapid grain growth. Second, uniformly distributed amorphous alumina provides a greater barrier effect for surface grains to fuse, providing a mechanism for amorphous alumina to suppress grain growth kinetically.

For comparing the heat resistance of LZO and L5AZO NFMs, the dynamic tensile strength and bending stiffness of the NFM are tested. Here, the mechanical properties of the LZO NFM and L5AZO NFM are compared (Fig. 5a). With the increase in heat cycling temperature, the strength of the LZO NFM decreases off a cliff until it is brittle fracture at 1100 °C. On the other hand, the L5AZO NFM exhibits excellent mechanical properties, and the strength not only does not decrease after thermal assessment, but also shows a slight increase at 1000 °C. Compare with other functional oxide fibers, the L5AZO NFM has advantages in mechanical properties and high-temperature resistance

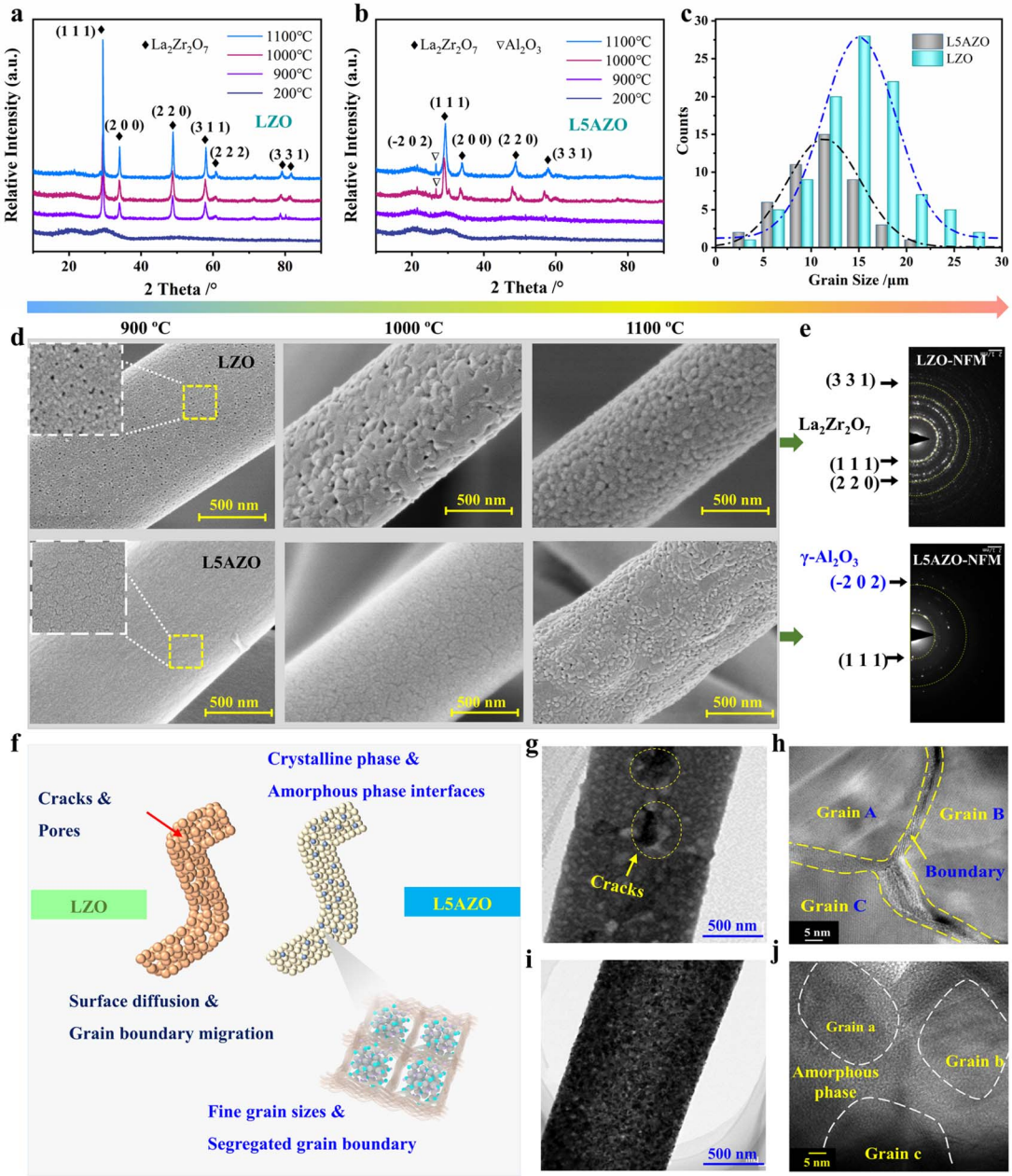

Fig. 4 Influence of the amorphous secondary phase on the high-temperature stability of LZO and L5AZO NFMs. Phase evolutions of (a) LZO and (b) L5AZO NFMs. (c) Statistical distribution of grain sizes. (d) Surface morphology evolution of the NFMs calcined at 900 °C,1000 °C, and 1100 °C for 1 h. (e) SEAD of LZO and L5AZO NFMs calcined at 1100 °C. (f) Schematic representation of the function of amorphous alumina. (g and h) TEM of the LZO NFM calcined at 1100 °C. (i and j) TEM of the L5AZO NFM calcined at 1100 °C.

(Fig. 5b)[40,41] In addition, the stiffness of the L5AZO NFM is measured and quantified with a paper softness tester, while a lower bending stiffness means better flexibility. After heat recycling twice at 1000 and 1100 °C, the L5AZO NFM shows significant softness and toughness that the traditional LZO NFM did not have. From the aspect of the membrane, when subjected to an external force, the nonconnective individual LZO NFs will slip relatively, which could improve the flexibility of the film. Interestingly, the hyperconnective LAZO NFM shows better ability during the bending and stretching process. But the rigidity of the LZO NFM cannot be obtained under a tensile force, because the NFM is brittle and cannot be bucked and deformed. The rigidity of he NFM is determined by the rigidity of ceramic NFs themselves. In contrast, the LAZO NFM treated at various temperatures has larger flexibility and bucking deformation under the condition of a small tensile force of 28.5 mN. Therefore, the rigidity of the NFM is affected by the deformation of the fiber itself and the fibril network deformation. Comparing the softness, the small softness (54.9 mN) of the LAZO NFM calcined at 1100 °C can be found, showing excellent flexibility (Fig. 5c).

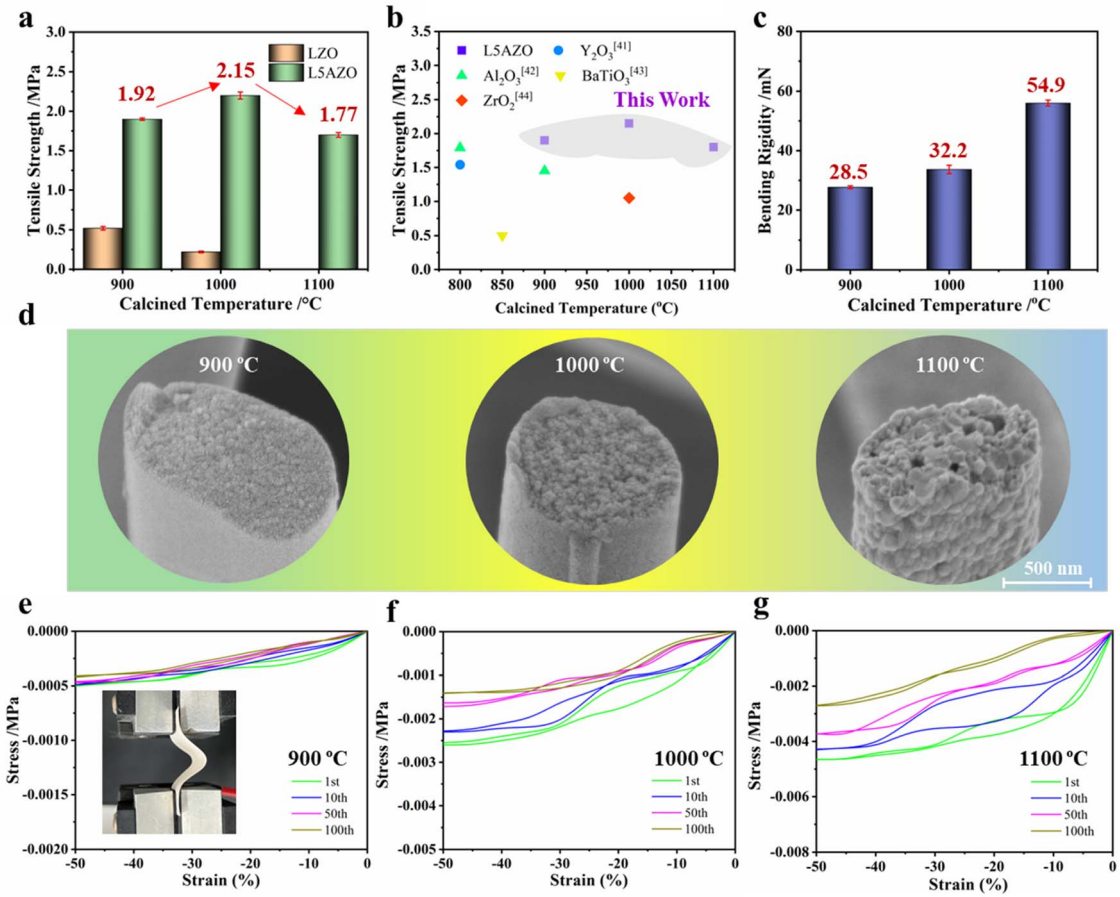

Fig. 5 Influence of the amorphous secondary phase on the high-temperature resistance of LZO and L5AZO NFMs. (a) Tensile strength of the NFM with different 3D structures. (b) The comparison of tensile strength with other studies.[42–45] (c) Bending rigidity of the L5AZO NFM after calcination. (d) Surface morphology of the L5AZO NFM after being calcined at 900 °C and retreated at 1000 °C and 1100 °C for 1 h, and (e, c, f) Tensile stress–strain curves of the L5AZO NFM under 100 cycles of compression.

Fig. 5d shows the tensile test fractures of the LAZO NFM at different temperatures. It can be seen that a small number of ultrafine holes appeared in the center area of the LAZO NFM after heat treatment at 1100 °C. The defects may result from the volume shrinkage caused by the transformation from the amorphous alumina phase into the crystalline phase, or the voids formed by grain rearrangement during sintering. The shape of holes is relatively regular, which does not have much negative impact on the mechanical strength of the NFM.

Most of the energy consumed in the bending process is used for the LAZO NFM deformation. With the increase in heat temperature, the adjustment of the LAZO NFM in a direction perpendicular to the load can be observed. The stiffness and stress of the hyperconnective LAZO NFM determined the stress of the whole membrane. Different from the nonconnective NFM, it is easier for individual nanofiber hinges with a narrower size distribution to disperse the complex stress in the hinge, and thus, they could improve the flexibility of the NFM as a whole. The initial stage of the LAZO NFM is an upper parabola compression curve with the slope constantly increasing, indicating that the membrane has a uniform force and a slight crease. With increasing testing cycles, the force on the membrane during deformation gradually decreased and tends to stabilize, which means that the membrane has super structural stability and mechanical properties. Correspondingly, the LAZO NFM showed strong plastic deformation ability and could produce 40–50% bending deformation under a 0.005 MPa pressure. After 100 cycles of compression, the plastic deformation ability remained stable. In addition, the typical tensile stress–strain curves of the LZO NFM are also tested, as shown in Fig. S9.† The LZO NFM could only produce a maximum compression deformation of 14%; otherwise, it will have a brittle fracture and could not be tested. The LAZO NFM showed a high mechanical strength of 1.97 MPa and a large strain of 1.42%. During a continuous 100 cyclic bending test (Fig. 4f), the membrane remained intact after bending 100 times (inset figure), indicating that the LAZO NFM has good flexibility and bending resistance.

Oxide ceramic fibers have been widely used in high-tech fields such as the environment, medical treatment, energy, and national defense. However, these oxide fibers are generally brittle and easy to fracture during bending deformation, which limits the service life and the expansion of subsequent application fields. How to enhance their flexibility, toughness and

high-temperature resistance at the same time is an urgent problem to be solved. Here, we proposed a strategy of refining grain sizes and forming a hyperconnective fibrillar network, and synthesized a new flexible L5AZO ceramic NF material with pyrochlore structures, which solved the bottleneck problem of large brittleness of multicomponent oxide ceramics at high temperatures. Here, flexibility refers to the ability to produce plastic deformation without fracture when the membrane is bent.

In summary, we have developed a kind of pyrochlore ceramic NFM with outstanding mechanical properties and high-temperature resistance originating from their hyperconnective fibrillar network with amorphous alumina. The theoretical models developed in this work accurately depicted the observed mechanical behaviors of the LAZO NFM, revealing quantitative relationships between configurations of fibrillar joints and macroscopic material properties. The mechanistic insights obtained from these models should be applicable to the engineering of a range of porous materials involving fibrillar networks. Further analysis will benefit from advanced characterization techniques revealing 3D topological details of microfibrillar networks, as well as sophisticated models including additional microstructural factors. From technological perspectives, the excellent mechanics, porosity, and manufacturability of these ceramic NFMs may create diverse opportunities for flexible electronics, energy systems, biomedical devices, and other applications.

4. Conclusion

We have reported a new kind of flexible and tough pyrochlore lanthanum zirconate nanofiber membranes with a hyperconnective network by combining ball-milling and *in situ* welding strategies with traditional electrospinning. The unique interactions between nanoscale constituents lead to assembled 3D networks with high nodal connectivity and strong welded connection between fibrils. These features lead to unusually high strength of the NFM, which is confirmed by our theoretical simulation of 3D fibrillar networks. The oxide nanofibers showed exceptional high-temperature stability and flexibility even after annealing at high temperatures. As numerous promising properties of oxide nanofibers rely on their nanoscale dimensions and nanocrystallinity, the mechanistic understanding and innovative bonding strategy developed in this work will pave the way for widespread applications of these important nanomaterials.

Conflicts of interest

The authors declare that they have no known competing financial interests or personal relationships that could have appeared to influence the work reported in this paper.

Acknowledgements

This work was supported by the China Postdoctoral Science Foundation (No. 2022M702443), National Defense Key Laboratory Foundation (WDZC20235250501) and Defense Industrial Technology Development Program (JCKY2017****).

References

1 H. Izumi and Y. Takashi, *Symmetry*, 2020, **12**(7), 1076.
2 Ö. Cihan, İ. Temizer, M. G. Gök and M. Karabaş, *Surf. Coat. Technol.*, 2020, **403**, 126437.
3 Z. Y. Shen, L. M. He, Z. H. Xu, R. D. Mu and G. H. Huang, *Surf. Coat. Technol.*, 2019, **357**, 427–432.
4 M. X. Jing, H. Yang, C. Han, F. Chen, W. Y. Yuan, B. W. Ju, F. Y. Tu, X. Q. Shen and S. B. Qin, *Ceram. Int.*, 2019, **45**, 18614–18622.
5 M. Y. Wei, J. Xu, R. W. Yang, J. T. Zhu, X. Y. Meng, J. L. Yang and F. Gao, *J. Am. Ceram. Soc.*, 2022, **105**, 4449–4456.
6 A. V. Kasyanova, A. O. Rudenko, Y. G. Lyagaeva and D. A. Medvedev, *Membr. Membr. Technol.*, 2021, **3**, 73–97.
7 X. S. Zhang, B. Wang, N. Wu, C. Han and Y. D. Wang, *Chem. Eng. J.*, 2021, **410**, 128304.
8 X. Y. Meng, J. Xu, J. T. Zhu, J. Zhao, M. Y. Wei, R. W. Yang and F. Gao, *J. Eur. Ceram. Soc.*, 2021, **41**, 6010–6017.
9 K. C. Khulbe and T. Matsuura, *J. Membr. Sci.*, 2020, **6**, 251–268.
10 W. X. Zheng, Y. F. Tang, Z. W. Liu, G. X. Xing and K. Zhao, *J. Mater. Chem. A*, 2022, **10**, 13544–13555.
11 X. H. Yan, X. Xiao, C. Au, S. Mathur, L. J. Huang, Y. X. Wang, Z. J. Zhang, Z. J. Zhu, M. J. Kipper, J. G. Tang and J. Chen, *J. Mater. Chem. A*, 2021, **9**, 21659.
12 N. Radacsi, F. D. Campos, C. R. I. Chisholm and K. P. Giapis, *Nat Commu*, 2018, **9**, 4740.
13 X. H. Li, Y. Y. Zhang, L. Zhang, S. H. Xia, Y. Zhao, J. H. Yan, J. Y. Yu and B. Ding, *Small*, 2022, **18**, 2106500.
14 Y. Y. Zhang, S. J. Liu, J. H. Yan, X. H. Zhang, S. H. Xia, Y. Zhao, J. Y. Yu and B. Ding, *Adv. Mater.*, 2021, 2105011.
15 L. Yao, W. Pan, J. Luo, X. H. Zhao, J. Cheng and H. Nishijima, *Nano Lett.*, 2018, **18**, 130–136.
16 F. Wu, Y. T. Liu, Y. Si, J. Y. Yu and B. Ding, *Nano Today*, 2022, **44**, 101455.
17 J. Pourasad, N. Ehsani and S. A. Khalifesoltani, *J. Eur. Ceram. Soc.*, 2016, **36**, 3947–3956.
18 X. S. Zhang, B. Wang, N. Wu, C. Han, C. Z. Wu and Y. D. Wang, *J. Eur. Ceram. Soc.*, 2020, **40**, 1877–1885.
19 Y. F. Wang, J. Han, J. P. Du, R. J. Liu and F. Wan, *J. Am. Ceram. Soc.*, 2021, **104**, 3508–3517.
20 J. Y. Li, H. Dai, Q. Li, X. H. Zhong, X. F. Ma, J. Meng and X. Q. Cao, *Mater. Sci. Eng., B*, 2006, **133**, 209–212.
21 J. X. Wang, X. T. Dong, Q. Z. Cui, G. X. Liu and W. S. Yu, *J. Nanosci. Nanotechnol.*, 2011, **11**, 2514–2519.
22 G. Ou, W. Liu, L. Yao, H. Wu and W. Pan, *J. Mater. Chem. A*, 2014, **2**, 1855.
23 M. X. Jing, H. Yang, C. Han, F. Chen, W. Y. Yuan, B. W. Ju, F. Y. Tu, X. Q. Shen and S. B. Qin, *Ceram. Int.*, 2019, **45**(15), 18614–18622.
24 M. S. Yu, S. C. Jesudass, S. Surendran, J. Y. Kim, U. Sim and M.-K. Han, *ACS Appl. Mater. Interfaces*, 2022, **14**, 31889–31899.

25 H. J. Tang, H. Y. Sun, D. R. Chen and X. L. Jiao, *Mater. Lett.*, 2012, **70**(1), 48–50.
26 W. J. Zhao, F. Yang, Z. L. Liu, H. Chen, Z. H. Shao, X. S. Zhang, K. X. Wang and L. Y. Xue, *Ceram. Int.*, 2021, **47**(20), 29379–29385.
27 Y. Zhao, J. H. Yan, W. P. Cai, Y. M. Lai, J. Song, J. Y. Yu and B. Ding, *Energy Storage Mater.*, 2019, **23**, 306–313.
28 J. Sharma, G. Polizos, C. J. Jafta, D. L. Wood III and J. L. Li, *J. Electrochem. Soc.*, 2022, **169**(5), 050527.
29 H. M. He, X. Wei, B. Yang, H. Z. Liu, M. Z. Sun, Y. R. Li, A. X. Yan, C. Y. Tang, Y. Lin and L. Z. Xu, *Nat Commu*, 2022, **13**, 4242.
30 C. P. Broedersz, X. M. Mao, T. C. Lubensky and F. C. MacKintosh, *Nat. Phys.*, 2011, **7**, 983.
31 A. Sharma, A. J. Licup, K. A. Jansen, R. Rens, M. Sheinman, G. H. Koenderink and F. C. MacKintosh, *Nat. Phys.*, 2016, **12**, 584.
32 A. Rosenflanz, J. Tangeman and T. Anderson, *Adv. Appl. Ceram.*, 2012, **111**(5–6), 323–332.
33 X. X. Zhang, X. T. Cheng, Y. Si, J. Y. Yu and B. Ding, *Chem. Eng. J.*, 2022, **433**, 133628.
34 M. Kumar, A. M. Isloor, T. S. Rao, A. F. Ismail, R. Farnood and P. M. G. Nambissan, *Chem. Eng. J.*, 2020, **393**, 124367.
35 A. S. Orekhov, N. A. Arkharova and V. V. Klechkovskaya, *Crystallogr. Rep.*, 2021, **66**(4), 699–703.
36 Y. Du, X. Wang, G. Z. Nie, L. J. Xu and Y. Hu, *J. Colloid Interface Sci.*, 2020, **580**(15), 234–244.
37 M. Alrefaee, U. P. Singh and S. K. Das, *Macromol. Symp.*, 2022, **402**, 1–6.
38 K. Heise, E. Kontturi, Y. Allahverdiyeva, T. Tammelin, M. B. Linder, Nonappa and O. Ikkala, *Adv. Mater.*, 2021, **33**, 2004349.
39 K. W. Li and G. A. Holzapfel, *J. Mech. Phys. Solids*, 2019, **126**, 226–244.
40 S. B. Lindström, D. A. Vader, A. Kulachenko and D. A. Weitz, *Phys. Rev. E: Stat. Phys., Plasmas, Phys. Rev. E: Stat., Nonlinear, Soft Matter Phys.*, 2010, **82**, 051905.
41 J. Jiang, N. Ni, W. W. Xiao, X. F. Zhao, F. W. Guo, X. H. Fan, Q. Ding, W. Hao and P. Xiao, *J. Eur. Ceram. Soc.*, 2021, **41**, 4264–4272.
42 Y. S. Xie, L. Wang, B. X. Liu, L. Y. Zhu, S. Shi and X. Wang, *Mater. Des.*, 2018, **160**, 918–925.
43 Y. Wang, W. Li, Y. Xia, X. Jiao and D. Chen, *J. Mater. Chem.*, 2014, **2**, 15124–15131.
44 C. Y. Pan, G. R. Xu, K. Xu, H. L. Zhao, Y. Q. Wu, H. C. Su, J. M. Xu and R. Das, *Sep. Purif. Technol.*, 2019, **221**, 44–63.
45 A. Stanishevsky, R. Yager, J. Tomaszewska, M. Binczarski, W. Maniukiewicz, I. Witońska and D. Lukas, *Ceram. Int.*, 2019, **45**, 18672–18682.